Thermal Effects in Field Electron Emission from Idealized Arrangements of Isolated and Interacting Micro-Protrusions

Darius Mofakhami[1,2], Benjamin Seznec[2], Tiberiu Minea[2], Philippe Teste[1], Romaric Landfried[1], and Philippe Dessante[1]

[1] Université Paris-Saclay, CentraleSupélec, CNRS, Laboratoire de Génie Electrique et Electronique de Paris, 91192, Gif-sur-Yvette, France.
[2] Université Paris-Saclay, CNRS, Laboratoire de physique des gaz et des plasmas, 91405, Orsay, France.
e-mail: darius.mofakhami@centralesupelec.fr

This is the version of the article before peer review or editing, as submitted by the authors to Journal of Physics D: Applied physics in october 2020*. IOP Publishing Ltd is not responsible for any version derived from it. The Version of Record is available online at* 10.1088/1361-6463/abd9e9

ABSTRACT

Modeling studies of thermo-field electron emission (TFE) from protrusions at a cathode surface usually use simulations in 2D axial symmetry. Indeed, time-dependent simulations in 3D are very demanding in computation time. Often, 3D simulations have been restricted to stationary pure field electron emission to account for the drastic current decrease caused by electric field screening when the emitters are close. Little interest has therefore been granted to the heat exchanges occurring between nearby emitters. Although the temperature is a second order parameter in TFE compared to the electric field, thermal effects become non-negligible in high current density regimes, where self-heating is well established. The present study focuses on the thermal effects occurring during the TFE from micro-protrusions. Our model considers a DC voltage, but solves in time the temperature evolution coupling the heat equation and the current continuity equation. The protrusions are modelled as hemiellipsoids with 2D axial symmetry. Emission enhancement due to the increase of the temperature in the thermo-field regime compared to the pure field regime is detailed as a test case for isolated protrusions. Then, full 3D simulations are used to investigate the thermal coupling between multiple neighbouring protrusions *via* their outwards heat fluxes inside the cathode. The results show a higher current increase due to thermal coupling for dome-like protrusions with low field enhancement factor. The current increases up to 13% of the total current for aspect ratios of 1 but this value is reached for an extreme applied electric field, hardly reachable in experiments. For sharper protrusions with higher field enhancement, the interaction range through the cathode being shorter, the thermal coupling is suppressed by electrostatic screening. Nevertheless, in arrangements of densely distributed field emitter, when the screening is compensated by a higher voltage, our model predicts the possibility of a moderate but noticeable thermal coupling even for sharp protrusions: a parametric study indicates up to 14.5% of the emitted current being caused by a thermal coupling through the cathode bulk, for protrusions with an aspect ratio of 10 under a fixed applied electric field of 0.4 GV/m in DC mode.

Key words. Thermo-field emission, Nottingham effect, 3D Modelling, Thermal coupling, Electrostatic screening, Field emitter array

Contents

1. Introduction

Field electron emission through quantum tunnelling from a conducting surface, under a strong electrostatic field, is a phenomenon that has led to important technological developments, chiefly for electron sources in microwave amplifier [Milne et al. 2006], flat panel display [Spindt et al. 1988] and X-ray generation devices [Sugimoto et al. 2010]. Besides, it is assumed to be part of the physical process causing vacuum arc ignitions in high-voltage devices, that limit for instance the performances of particle accelerators [Timko et al. 2015]. Nevertheless, the considerable magnitude required for the electric field to allow field emission, several gigavolts per meter, makes it essentially observable at the apex of sharp protrusions, where the electric field is significantly enhanced by the compression of the isopotentials [Utsumi 1991; Sarkar and Biswas 2019]. Emission from the surface around the apex generates a current inside

the protrusion. Above a certain current density, both the Joule heating and the Nottingham effect [Nottingham 1941] can cause a temperature increase, respectively inside the protrusion and at its surface. This self-heating mechanism causes a transition from pure field emission to thermo-field emission (TFE). Higher temperatures then facilitate the electron emission, causing even more ohmic heating. Under sufficiently high applied electric field, the self-heating mechanism can degenerate into a thermo-emissive instability causing a voltage breakdown [Vibrans 1964; Bocharov and Eletskii 2007]. Otherwise, a steady state may be reached through an efficient heat sinking towards the cathode bulk, and a cooling Nottingham effect once the Nottingham temperature has been reached [Charbonnier et al. 1964]. This thermal equilibrium corresponds to steady distributions of current density and temperature.

The phenomenon of electron emission from a field-enhancing protrusion was already studied in the early 50's [Dyke et al. 1953a], with building equations established some decades earlier [Fowler and Nordheim 1928]. Due to its complex nature the physics involved could not, however, be fully grasped by analytical calculations and has therefore remained challenging. Two decades ago, numerical simulations have extended the prediction capabilities of the theoretical models established in the twentieth century. Solving systems of coupled differential equations in 1D or 2D with axial symmetry, they have, among others, shed light on the self-heating process of single field emitters [Su et al. 1993; Ancona 1995; Rossetti et al. 2002]. The more recent growth in computing power makes it possible to go further: 3D finite-element solvers allow to track the heating process of multiple emitters and their interactions, up to thermal instability or equilibrium, *via* time-dependent simulations. For a single emitter, it is clear that the evolution through self-heating at high enough current density from initially pure field emission to thermo-field emission would lead to an increase of emitted current. In the case of multiple emitters in close proximity, the individual emitted current would be damped by electrostatic screening. Under appropriate electric field, however, high density of emitters could lead in some area to localized heat overflows, which would then enhance the emission *via* an increase in temperature. This possible coupling of heat fluxes between close protrusions can boost the electron emission and will be here referred to as *thermal coupling*.

The aim of this paper is first to better characterize the transition towards the thermo-field regime over the applied electric field range and then to explore the possibility of thermal coupling. To this end, our simulation routine uses our own TFE model, following the approach proposed by [Murphy and Good 1956], to compute the emitted current density as a function of the electric field and temperature at the surface of the protrusions, in addition to the work function. The routine uses the Laplace equation to compute the electric field and solves the time-dependent heat and current equations inside the protrusion. These equations are solved in 3D *via* a finite-element approach using the COMSOL Multiphysics software (5.4) [COMSOL 2020]. This way, the routine not only take into account the electrostatic screening in the inter-electrode space, but also the possible thermal coupling occurring in the cathode volume. Last, the protrusions are modelled by axi-symmetric hemiellipsoids. An example of simulation result for two hemisphere protrusions is shown on figure 1. More details are given in section 2.
The study is then divided in two parts, respectively in section 3 and 4. The first part focuses on single protrusions modelled in 2D: the thermal contributions to the emission is quantified over a broad range of applied electric field in DC, up to the pre-breakdown voltage. This allows to determine the relevant range of parameters where thermal coupling can occur. In the second part, 3D simulations are used to characterize thermal coupling between multiple protrusions, searching for the upper limits to its contribution to the emitted current.

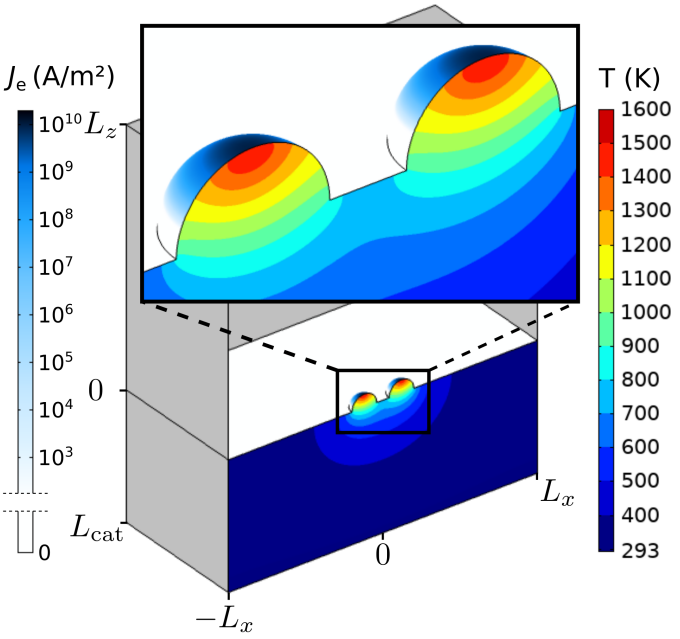

Fig. 1: Example of a 3D simulation performed with COMSOL Multiphysics using our thermo-field emission model for two identical hemispheres under an applied electric field of $1.9\,GV/m$. The color map on the upper surface of the cathode displays the current density variations (colorbar on the left), while the color map along the vertical cut shows the temperature levels (colorbar on the right).

2. Model

This work takes advantage of the high performance of nowadays numerical solvers of differential equations using a 3D finite-elements approach. It is here used to simulate the TFE of well-defined protrusions, distributed at the surface of a cathode and immersed in a homogeneous DC electrostatic field. The corresponding system of equations couples the electron emission with the current continuity equation and the heat balance. It is time-dependent and highly non-linear and therefore needs to be solved numerically in 2D and 3D.

2.1. Geometry

The protrusions are here modelled as axi-symmetric hemiellipsoids. The main parameters relative to the geometric configuration are thus the height H_i and the base radius R_i of each ellipsoidal emitter, the corresponding aspect ratio $f_i = H_i/R_i$, and the positions of their respective symmetry axis in the upper plane of the cathode. The cathode surface, including the protrusions surface, is called Σ.

When considering only two emitters, the space of parameters can be reduced to $\{H_1, f_1, H_2, f_2, d\}$, where d is the distance

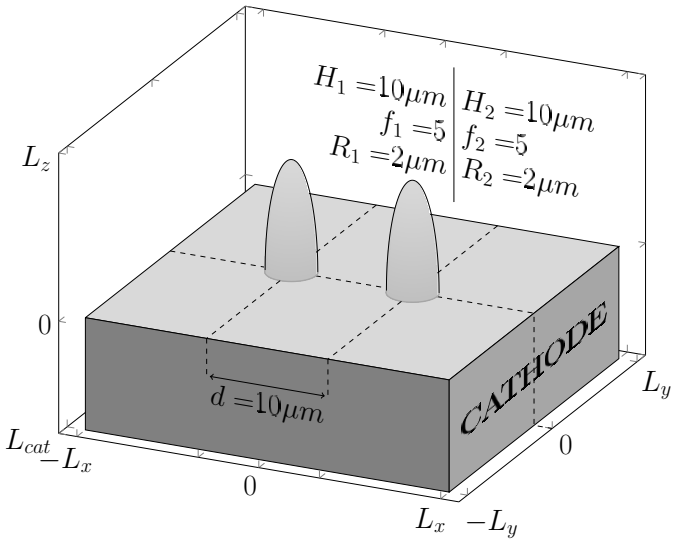

Fig. 2: Example of parameter values for a given arrangement of two identical tips. H and R respectively indicate the height and the base radius of the protrusion. $f = H/R$ denotes the aspect ratio. The simulation domain limits L_x, L_y, L_z and L_{cat} are not at scale here.

between the symmetry axis of the two emitters (figure 2). Note that R_1 and R_2 are set *via* f_1 and f_2 respectively.

Protrusions are placed in a volume domain bounded by $\pm L_x$ in the x direction, $\pm L_y$ in the y direction, and $\{-L_{\text{cat}}, L_z\}$ in the z direction. These bounds are chosen so that they do not influence the physics, but their impact on computation time is limited. A good compromise is obtained with L_x, L_y, L_z and L_{cat} of the order of a few dozen times the height of the highest protrusion.

2.2. Details of the electron emission model

- Inside the protrusion, the electrons are described by a Fermi-Dirac statistic. Their energy distribution depends on the protrusion equilibrium temperature T and its work function φ. At the protrusion surface Σ, the vacuum-metal interface is modelled by the usual step potential barrier.
- In the inter-electrode space, the solving of the electrostatics gives the electric field distribution in vacuum.
- Next, the electric field norm F at the protrusion surface Σ is taken into account together with the image charge correction to compute the actual electron potential barrier.
- The transmission probability $D(F, \epsilon)$ of an electron of energy ϵ through the barrier is computed by solving Schrödinger equation in 1D using the Wentzel-Krammers-Brillouin (WKB) approximation. Curvature effects are therefore not taken into account, as they have been shown to be negligible for apex radius larger than a few nanometers [Kyritsakis and Xanthakis 2016].
- To then get the emitted current density $J_e(F, T, \varphi)$ from $D(F, \epsilon)$ the elliptical functions involved are computed numerically and the result is integrated over ϵ. If the electric field is high enough over the protrusion apexes, electrons around the Fermi energy level are able to escape the metal through quantum tunnelling and a current is extracted.
- The emitted current causes Nottingham effect at the protrusion surface. The corresponding Nottingham thermal flux Φ_N is computed by accessing the mean energy difference W_N between the emitted electrons in vacuum and the replacement electrons from the bulk [1] :

$$\Phi_N(F, T, \varphi) = \frac{J_e(F, T, \varphi)}{-e} \times W_N(F, T, \varphi) \tag{1}$$

- In the same time, inside the protrusions, the establishment of a current leads to Joule heating. As a consequence, the temperature increases along the protrusions axes. If the initial current density is high enough, the emitter may then enter the thermo-field emission regime where the increase in temperature causes additional thermionic electron emission, yielding even more extracted current.
- This positive feedback loop between Joule heating and current is then counterbalanced over time by a heat sinking towards the cathode bulk – assumed here acting as a thermostat kept at 300 K – and in addition a cooling Nottingham effect if the Nottingham temperature is exceeded.
- When a steady state is reached, the equilibrium distributions of the local variables, such as the current density and the temperature, are accessible as well as the global variables like the intensity of the total emitted current.

2.3. Electrostatics model

To compute the electrostatic field at the emitters surface, the Laplace equation for the potential V_{out} is solved in the inter-electrode gap, assumed to be perfect vacuum:

$$\Delta V_{\text{out}} = 0\,, \quad \boldsymbol{F} = -\boldsymbol{\nabla} V_{\text{out}} \tag{2}$$

where V_{out} and $\boldsymbol{F}$ respectively denote the electric potential and field. The corresponding boundary conditions (BCs) are the following. At the cathode surface Σ (see the green dashed line on figure 3), a Dirichlet BC sets the V_{out} to the macroscopic applied potential V_0. At the upper limit of the simulation domain for $z = L_z$ a von Neumann BC sets the field norm F to the applied electric field $E_0 = V_0/D_{\text{gap}}$, where D_{gap} is the distance separating the anode from the cathode. On the far left and right sides, where $x = \pm L_x$ or $y = \pm L_y$, symmetry von Neumann BCs are enforced on the electric field.

$$V_{\text{out}}\big|_{\Sigma} = V_0\,, \quad \boldsymbol{F}\big|_{Lz} = \boldsymbol{E_0}\,, \quad \boldsymbol{F}\big|_{\pm Lx}^{\pm Ly} \cdot \boldsymbol{n} = 0\,, \tag{3}$$

From the local electric field norm F at position $\boldsymbol{r}$ on the protrusion surface, the Field Enhancement Factor (FEF) is defined by:

$$\beta(\boldsymbol{r}) = \frac{F(\boldsymbol{r})}{E_0} \tag{4}$$

while its specific value at the apex of a protrusion (apex FEF) writes:

$$\beta_a = \frac{F_a}{E_0} \tag{5}$$

[1] One should note that the Nottingham effect plays a tricky role in the cathode heating process. The replacement electron energy is typically of the order of the Fermi energy ϵ_F. When emission happens at low temperature, emitted electrons are essentially distributed at energy equal or lower than ϵ_F, so the resulting Nottingham flux will heat the cathode. But as temperature increases, the emitted electron mean energy will rise as well and the Nottingham heat flux will thus decrease until it eventually becomes negative, and thus cool the protrusion, for temperatures beyond the so-called Nottingham threshold temperature [Charbonnier et al. 1964].

with F_a the field value at the apex. The FEF is defined for an isolated protrusion, *i.e.* not interacting with any other protrusions. It is defined here as an intrinsic property of the protrusion, directly related to its geometry.

Note that field modification due to space charge during the emission is neglected at present. The interested reader can consult [Dyke et al. 1953b] (experimental) or [Zhu and Ang 2015; Seznec et al. 2020] (modelling).

2.4. Electric model

Inside the cathode, charge conservation must be satisfied:

$$\boldsymbol{\nabla} \cdot \boldsymbol{j} = 0 \tag{6}$$

with the current $\boldsymbol{j}$ expressed in the form of the gradient of V_{in}:

$$\boldsymbol{j} = \left(\sigma(T) + \epsilon_0 \frac{\partial}{\partial t}\right) \boldsymbol{\nabla} V_{\text{in}} \tag{7}$$

where V_{in} denotes the local potential inside the cathode and its gradient is obviously related to the electron emission. The equation resulting from (6) and (7) is solved with the following BCs:

$$V_{\text{in}}\big|_{Lcat} = V_0\,, \quad \boldsymbol{j}\big|_{\Sigma} \cdot \boldsymbol{n} = J_e(F,T,\varphi)\,, \quad \boldsymbol{j}\big|_{\pm Lx}^{\pm Ly} \cdot \boldsymbol{n} = 0\,, \tag{8}$$

Note that according to (7), the electron emission J_e at Σ implies a small voltage loss along the axis of the protrusions so that $V_{\text{in}}|_{\text{apex}} < V_{\text{in}}|_{Lcat}$. This loss is amplified by higher current density and electric resistivity as often observed for carbon emitters [Minoux et al. 2005]. In our case however, simulations use typical metal conductivities of the order of 10^6 to 10^7 S/m. Moreover, as a distance of $D_{\text{gap}} = 200\mu m$ is chosen between the two electrodes, the voltage applied in our simulations is around 10 to 100 kV. The relative loss of voltage is therefore completely negligible, of the order of 10^{-6}, leading to $V_{\text{in}}|_{\text{apex}} \lesssim V_0$. This is why the electrostatics inside the enclosure can be solved only once assuming $V_{\text{out}}|_{\Sigma} = V_0$ all over the cathode surface, as presented in subsection 2.3.

2.5. Heat transfer model

The electron emission causes Joule heating inside the protrusion and Nottingham heat fluxes at their surface. The thermalization of the cathode is then described by the following heat equation:

$$\mu(T)c(T)\frac{\partial T}{\partial t} - \boldsymbol{\nabla} \cdot \boldsymbol{\phi} = \frac{j^2}{\sigma(T)}$$
$$\boldsymbol{\phi} = -\kappa(T)\boldsymbol{\nabla} T \tag{9}$$

with T the temperature, $\boldsymbol{\phi}$ the corresponding heat flux, μ, c, κ and σ respectively the volume mass density, the specific heat capacity, the thermal conductivity and the electrical conductivity of the cathode material, all being temperature-dependent.

In all the results of the present paper, the cathode bulk is assumed big enough to act as a thermostat beyond L_{cat}. At the interface Σ, cooling or heating flux condition is fixed by the Nottingham effect Φ_N. On the far left and right sides of the simulation domain, symmetry von Neumann BCs are set. These BCs are summarized by the following equations:

$$T\big|_{Lcat} = 300\ K\,, \quad \boldsymbol{\phi}\big|_{\Sigma} \cdot \boldsymbol{n} = \Phi_N(F,T,\varphi)\,, \quad \boldsymbol{\phi}\big|_{\pm Lx}^{\pm Ly} \cdot \boldsymbol{n} = 0\,, \tag{10}$$

Note that at the emitter surface, no radiation losses are taken into account as they were found to be negligible compared to the conductive heat evacuation at the protrusions bases. Over the parameters range of interest, an upper estimation can be obtained assuming black body radiation:

$$10^{-4} < \frac{\iint \sigma^\star T^4\big|_{\Sigma} \mathrm{d}S}{\iint \boldsymbol{\phi} \cdot \boldsymbol{n}\big|_{z=0} \mathrm{d}S} < 10^{-3} \tag{11}$$

where $\sigma^\star = \frac{2\pi^5 k^4}{15h^3c^2}$ is the Stefan-Boltzman constant.

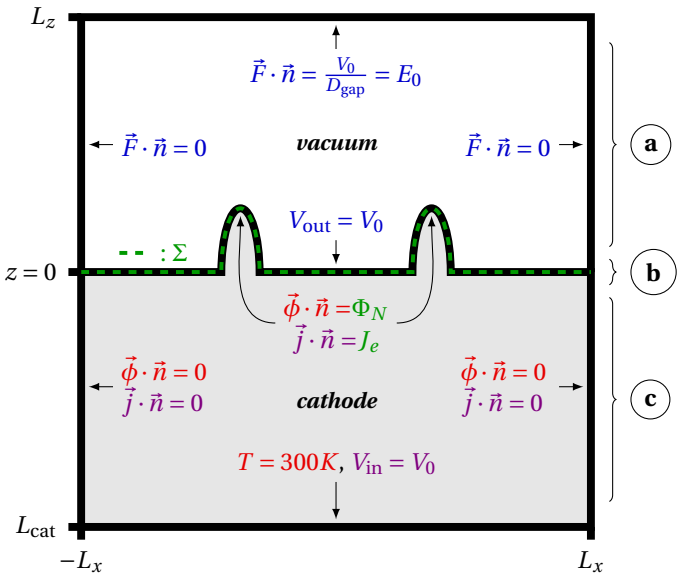

Fig. 3: Boundary conditions in a 2D sectional view of the 3D simulation domain along the x-axis (*the dimensions are not at scale*). **a**: Electrostatic field equation is solved once in the vacuum. **b**: Our electron emission model is updated at each time step at the cathode surface Σ. **c**: Heat and current equations are solved together at each time step in the cathode (including protrusions).

2.6. Simulation algorithm

A complete simulation corresponds to the chart-flow depicted in figure 4. To get the electric field at the protrusions surface, the electrostatics are only solved once using a static finite-element methode (FEM) included in COMSOL Multiphysics (5.4) [COMSOL 2020]. Using this software, the coupled electric and heat equations are then solved together using a time-dependent FEM and a nonlinear solver (Newton-Raphson) to get the current density and temperature distributions. These distributions are updated at each time step by computing the value of the emitted current density $J_e(F,T,\varphi)$ and the Nottingham heat flux $\Phi_N(F,T,\varphi)$ for the BCs, *via* our electron emission model written in Fortran. The simulation stops when a steady state is reached.

The model is versatile in the sense that it is able to follow the electron emission of any 3D configuration of any number N of protrusions of any shape, of course at the cost of a computation time increasing with both N and the shape complexity.

3. Thermal effects in the field emission of a single protrusion

The results presented here focus on the influence of thermal effects in field electron emission from idealized protrusion with

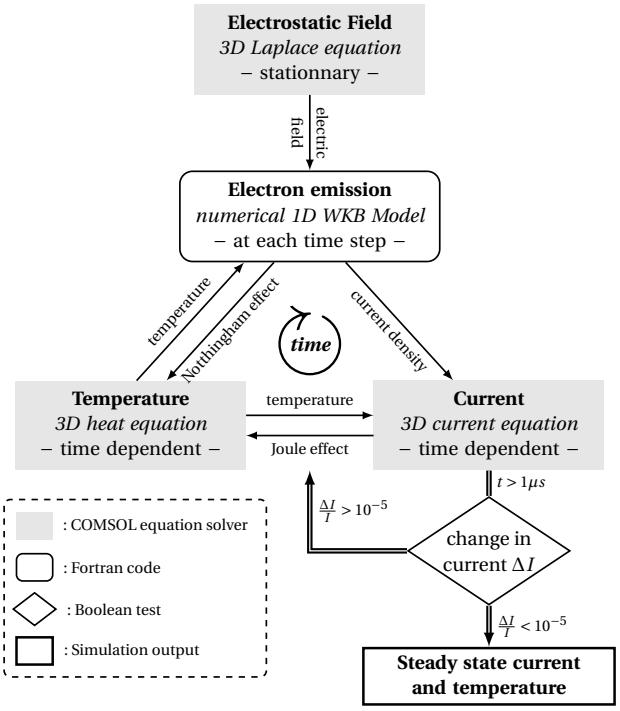

Fig. 4: Chart flow of the successive simulation steps.

hemiellipsoidal shape. Overall insights on the heating process of a single protrusion are given, in order to characterize the transition from the pure field emission regime to the thermo-field emission (TFE) regime. Because only one emitter is here considered, the x and y coordinates described in the model section are merged in a radial coordinate r and the simulation domain is reduced to a 2D box with axial symmetry (see the model described in [Seznec et al. 2016], section 2 therein). This dimension reduction eases the exploration of thermal effects over a large range of applied electric field. Besides, it offers the possibility to extract the more relevant parameters to then study thermal coupling (sec. 4), which on the contrary do require a 3D modelling.

In the present work, the space of parameters is reduced to the aspect ratio f by setting the protrusion height to $H = 10\,\mu m$. The results focus on aspect ratio from 1 to 10, especially $f = 1$, $f = 2$, $f = 5$, and $f = 10$ in this section, corresponding respectively to an apex FEF of $\beta_a = 3$, $\beta_a = 5.76$, $\beta_a = 17.9$, and $\beta_a = 49.3$. Besides, our simulation are usually performed with three metals, namely tungsten, molybdenum or titanium. Hereafter in this document, all the results presented are obtained with titanium: average work function $\varphi = 4.3\ eV$, fusion temperature $T_F = 1941\ K$, and conductivities $\sigma(T)$ and $\kappa(T)$ set according to the fitting polynomials proposed for titanium in [Milošević and Maglić 2008] and [Ho et al. 1972] respectively.

3.1. Transition to the thermo-field emission regime

The details of the variation of the current with the voltage is difficult to predict and a complete simulation is therefore usually required for each different arrangement. The causal link between the emission and the voltage, however, is simple: the higher the applied voltage V_0 is, the more current is extracted. In particular, one can fairly predict that at some applied voltage the current density inside the protrusion should be high enough to induce a noticeable increase of temperature *via* the Joule heating and/or a heating Nottingham effect. There would then be a transition over the applied voltage from pure field electron emission (low current density, constant temperature) to thermo-field electron emission (high current density, self-heating process). If the voltage – and so the related current density – is high enough, the equilibrium temperature distribution resulting from the self-heating process may reach the fusion temperature T_F at some location. This pre-breakdown condition is necessary (eventhough not always sufficient) to cause a thermal instability, that may then degenerate into a vacuum breakdown, in accordance with the processes described for example in [Davies and Biondi 1971], [Fursey 1985], [Batrakov et al. 1999]. However, our model does not include the physics that describe such a phenomenon. It is only valid up until the pre-breakdown phase, where the maximum temperature in the protrusion just reaches the melting temperature. This occurs for a threshold electric field denoted E_0^{pb} that is produced by an applied voltage considered hereafter – for simplification – as the pre-breakdown voltage: $V_0^{\mathrm{pb}} = E_0^{\mathrm{pb}} \times D_{\mathrm{gap}}$. Thus, E_0^{pb} is the minimum applied field for which the fusion temperature is reached somewhere in the cathode ($T_F = 1941\ K$ for Titanium). In order to guarantee the integrity of the protrusions, the field values in the simulations are restricted to $E_0 \leq E_0^{\mathrm{pb}}$: the applied voltage never goes beyond the pre-breakdown voltage.

The emitted current I_{pb} when E_0^{pb} is applied is therefore the maximum current one can extract from a single protrusion before it begins to melt. This field value is therefore used to define the emission range of a single protrusion $\Delta E_0 = [E_0^{\mathrm{min}}, E_0^{\mathrm{pb}}]$, where E_0^{min} is defined as an arbitrary lower limit for which the protrusion emits one thousandth of I_{pb}.

Over this emission range, the transition from cold to thermo-field regime is explored for four typical protrusions, $f = 1$, 2, 5 and 10, *via* the following global quantities :

- The self-heating of the protrusion in terms of the mean value of the Joule and Nottingham heating in relation to the the protrusion volume V :

$$\mathcal{P}_J = \frac{1}{V}\iiint_V P_J \mathrm{d}\tau \quad \text{and} \quad \mathcal{P}_N = \frac{1}{V}\iint_\Sigma \Phi_N \mathrm{d}S \tag{12}$$

- The maximum temperature at equilibrium in the protrusion volume :

$$T_{\max} = \max_V(T) \tag{13}$$

- The total emitted current :

$$I(F,T) = \iint_\Sigma J_e(F,T)\mathrm{d}S \tag{14}$$

- And the relative gain in current due to the increase in temperature :

$$g_I = \frac{I(F,T) - I(F,300K)}{I(F,300K)} \tag{15}$$

All these global quantities introduced by equations 12 to 15 are depicted *versus* the applied electric field on figure 5. Taking advantage of the different aspect ratios considered, the results for each protrusion are displayed on the same x-axis. Each data point at a given E_0 corresponds to a 2D axi-symmetric transient simulation whose quantities are evaluated at thermal equilibrium (steady state).

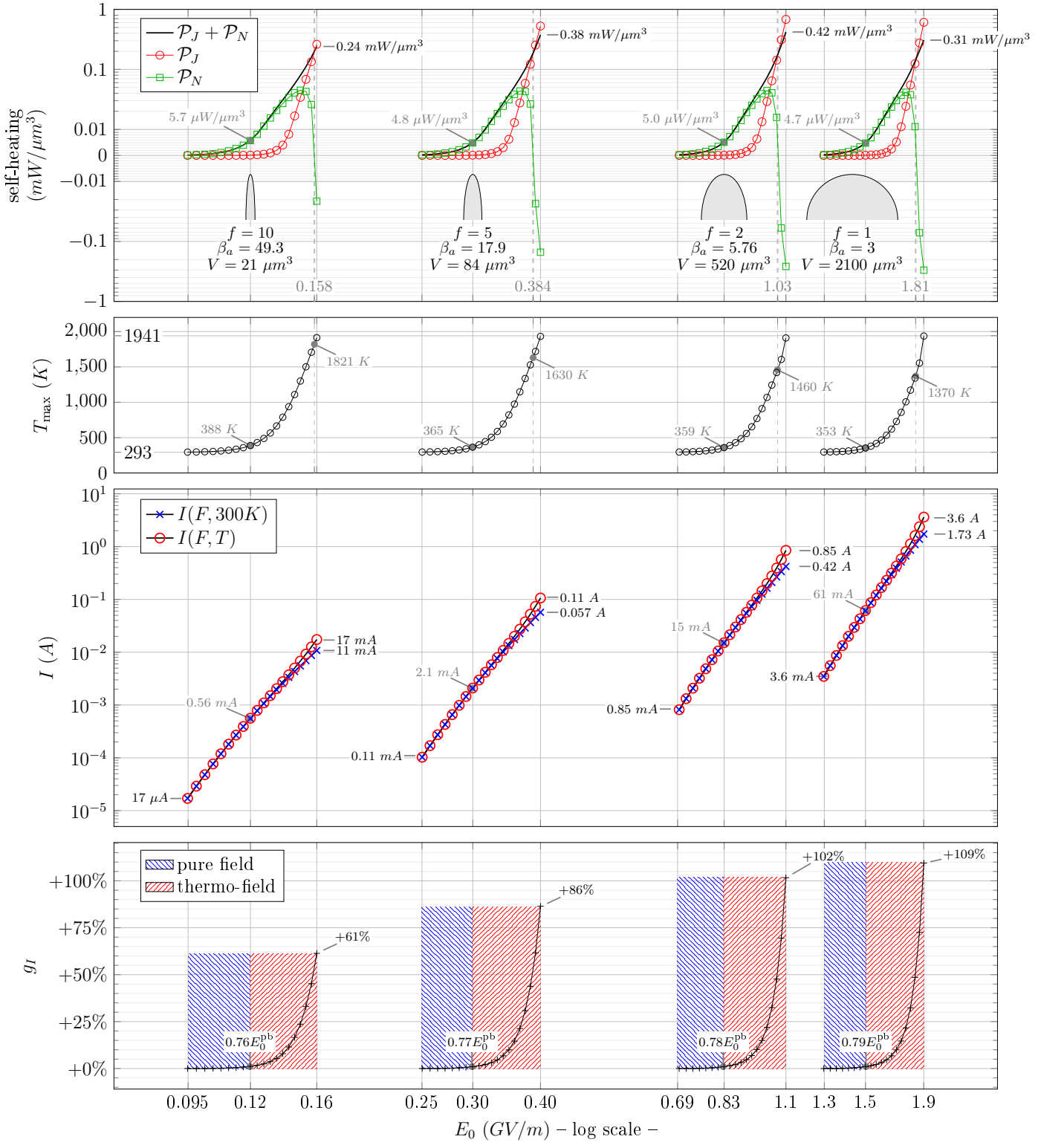

Fig. 5: Variation of the global quantities of equations 12 to 15 *versus* the applied electric field E_0 over the range $\Delta E_0 = [E_0^{\min}, E_0^{pb}]$ for aspect ratios $f = 1, 2, 5$ and 10.

• The first panel gives the variation of the averaged Joule heat $\mathcal{P}_J$ and Nottingham heat $\mathcal{P}_N$. The total heat $\mathcal{P}_J + \mathcal{P}_N$ is explicitly displayed at $g_I = 1\%$ (see bottom panel, hatch separation) and at E_0^{pb}. A vertical dashed line highlights the Nottingham inversion. Note that the y-axis is in symlog scale: linear between -0.01 and 0.01 and logarithmic beyond. The insets show the shape of each considered protrusion with its aspect ratio, apex FEF and volume.

• The second panel shows the increase of the maximum temperature T_{max} inside the protrusion. The temperatures at $g_I = 1\%$ and at the Nottingham inversion are explicitly displayed.

• The third panel presents the current emitted from the protrusion assuming cold emission only: $I(F, 300K)$ and the total current when the thermo-field emission supplement the current: $I(F, T)$. The values at $E_0^{\min}$ and E_0^{pb}, as well as the value at $g_I = 1\%$ are explicitly displayed.

• The last panel gives the relative gain in current due to the temperature increase, *i.e.* the relative discrepancy between the above curves for $I(F, 300K)$ and $I(F, T)$. A separation at $g_I = 1\%$ is highlighted by blue and red hatches to arbitrary delimit the pure field regime from the thermo-field regime. The corresponding field value is given in line with the pre-breakdown field E_0^{br} for each aspect ratio f.

The first panel of figure 5 shows the respective contribution of the Nottingham effect and the Joule heating in the thermal equilibrium at different applied electric field. It is interesting to notice that for low and medium values of applied field, the Nottingham effect contributes alone to the heating. This is consistent with the results of [Su et al. 1993] [2] and [Ancona 1995] [3]. It is only at high electric field (*i.e.* high enough emitted current) that the averaged Joule heating catches up, where the averaged Nottingham heating reaches a maximum. For even higher field values, the averaged Nottingham effect decreases (and can then be cooling) while the ohmic heating takes over and bring the tip closer to breakdown. Note however that the overall heat surplus $\mathcal{P}_J + \mathcal{P}_N$ is always compensated by the heat sinking, as all of the presented results come from simulations that have reached a thermal equilibrium.

The second panel shows the continuous increase of the protrusion maximum temperature toward the fusion temperature $T_F = 1941\ K$, as a result of the self-heating process. The field values E_0^{Nh} for which $\mathcal{P}_N = 0$ are highlighted by extra x ticks on the first panel and the corresponding maximum temperatures T_{Nh} are given on the second panel (see the dashed gray lines). The values are also summarized in table 1. Remarkably, the averaged Nottingham effect reverses at smaller temperature for smaller aspect ratio f. This is the consequence of a smaller local electric field at the emission surface as will be shown in subsection 3.2.

To assess the contribution to the current of the increase in temperature, two sets of results are compared in the third panel. The first set corresponds to electrostatics-only simulations, *i.e.* cold emission only. In this case the current $I(F, 300\ K)$ is obtained by setting the temperature at 300 K all over the emitting surface (blue crosses - Fig. 5 - 3rd panel). On the contrary, the second set comes from a complete solving of the model, as described in fig. 4, and the computation of the current $I(F, T)$ uses the whole equilibrium temperature distribution at the emitting surface (red circles - Fig. 5 - 3rd panel). When the applied electric field is much lower than the pre-breakdown field E_0^{pb} no distinction can be made between the two curves. However, closer to E_0^{pb} a difference appears that witnesses a gain in current g_I due to the addition of the thermionic mechanism for electron emission. This corresponds to the thermo-field emission regime.

The last panel displays $g_I(E_0)$ which is the relative discrepancy between the red curve $I(F, T)$ and the blue one $I(F, 300\ K)$ of the third panel. For $f = 10$ the gain on the current goes up to $g_I = +61\%$ over the applied electric field range $\Delta E_0 = [0.095, 0.16]\ GV/m$. For $f = 1$ it reaches $g_I = +109\%$ over a relatively smaller range, $\Delta E_0 = [1.3, 1.9]\ GV/m$. This tends to show that the rounder the protrusions are, the more thermo-field effects contributes to the emission.

Besides, $g_I(E_0)$ is the perfect quantity to distinguish the pure field electron emission regime ($g_I \sim 0$) from the thermo-field regime ($g_I > 0$), as it directly quantifies the contribution of the thermal effects to the current. By setting an arbitrary limit between the two regime at $g_I = 1\%$, a separation appears for each f at applied field between 0.75 to $0.80 E_0^{\mathrm{pb}}$ with a corresponding heating around $\sim 5\ \mu W/\mu m^3$. The applied field corresponding to this separation is denoted $E_0^{1\%}$. Because the self heating of protrusions is more directly related to the current – both for Nottingham and Joule heating – it is interesting to read this limit in terms of current per unit volume. Dividing the current values given on the third panel at the 1% separation by the protrusions volume V shown on the insets of the first panel, one gets a similar value for each protrusion, between 25 and 30 $\mu A/\mu m^3$ (thermal effects are still too small to make a clear difference). Doing the same computation at the pre-breakdown voltage, however, leads to a more readable distinction between protrusions, I_{pb}/V increasing from 810 $\mu A/\mu m^3$ for $f = 10$ to 1700 $\mu A/\mu m^3$ for $f = 1$. Values are given in table 1. From this result it appears that rounded protrusions require more current per unit volume to heat up to the breakdown. This can be mainly related to the fact that rounder protrusions have a better heat sinking at their base, also meaning a temperature increase that radially spreads wider. This assertion is developed in the next subsection.

Quantity	Unit	$f = 10$	$f = 5$	$f = 2$	$f = 1$
E_0^{Nh}	GV/m	0.158	0.384	1.03	1.81
T_{Nh}	K	1821	1630	1460	1370
$E_0^{1\%}$	GV/m	0.12	0.30	0.83	1.5
$I_{1\%}/V$	$\mu A/\mu m^3$	27	25	29	29
E_0^{pb}	GV/m	0.16	0.40	1.1	1.9
I_{pb}/V	$\mu A/\mu m^3$	810	1300	1600	1700

Table 1: Comparison between the different aspect ratios of quantities related to the thermo-field transition. The meaning of these quantities is explained in the manuscript.

3.2. Details of the emission in the thermo-field regime

The self-heating process has been shown to differ between protrusions depending on their aspect ratio f. To better understand this, it is of interest to look at the distributions of the local variables F, T, and $J_e(F, T)$ at $E_0 = E_0^{\mathrm{pb}}$. Figures 6 and 7 displays these distributions for $f = 1, 2$ and 5.

The first panel of figure 6 shows the field distribution at pre-breakdown voltage, so for applied field $E_0 = E_0^{\mathrm{pb}}$. Although E_0^{pb} is higher for lower aspect ratio, the graphs highlight that the local field value at the apex F_a is smaller for lower aspect ratio while the field enhancement spreads over a larger surface. Hence, for smaller aspect ratio, the emission occurs at lower field values but over a larger surface around the apex. This is measurable *via* the introduction of the radius $R_{90\%}$ defining, for an axi-symmetric situation, the protrusion surface around the apex that emits 90% of the total current:

$$\int_0^{R_{90\%}} 2\pi r C(r) J_e(F, T) \mathrm{d}r = 0.9 \times \int_0^{R} 2\pi r C(r) J_e(F, T) \mathrm{d}r \qquad (16)$$

with

$$I(F, T) = \int_0^{R} 2\pi r C(r) J_e(F, T) \mathrm{d}r \qquad (17)$$

being the total extracted current and

$$C(r) = \sqrt{1 + \frac{H^2 r^2}{R^4 - r^2 R^2}} \qquad (18)$$

[2] See in particular fig. 9 of the corresponding paper. The cited work models a 2D axial symmetry gated field emission triode, with an emitter height of the order of 1 μm.

[3] In this reference, however, the ohmic heating is found to be negligible even at relatively high emitted current. We assume this is related to the protrusion height below 0.5 μm leading to a very small volume over surface ratio, working against the ohmic heating.

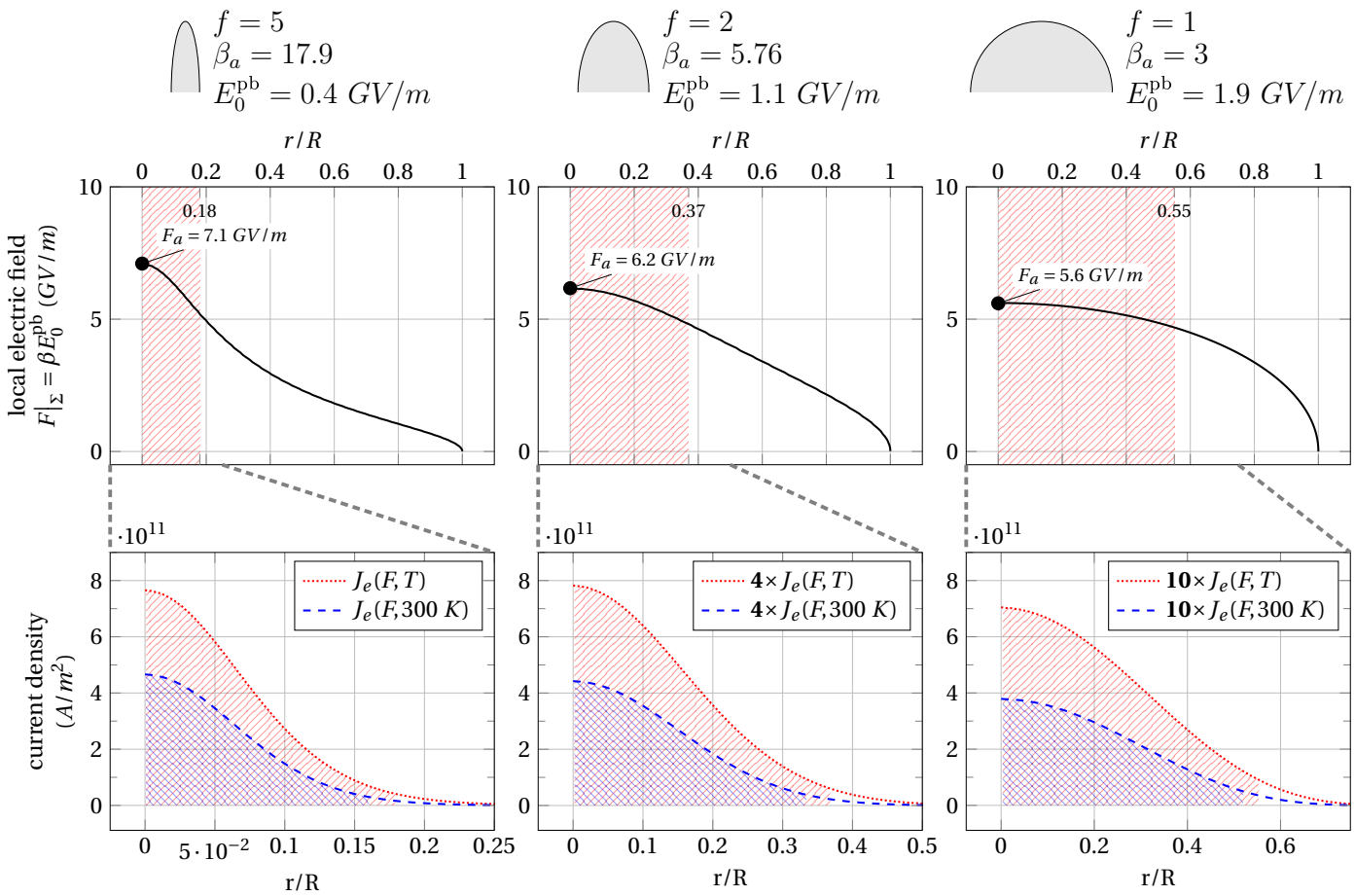

Fig. 6: 2D axi-symmetric emission of single protrusions with aspect ratio $f = 5$, $f = 2$ and $f = 1$ when the corresponding pre-breakdown field E_0^{pb} is applied. The upper schemes recall the protrusion properties. The graphs of the first row compares the radial distribution of the local electric field over the whole protrusion, from $r = 0$ to $r = R$ with a common y-axis. F_a corresponds to the local electric field at the apex. The second row of graphs presents the distribution of the emitted current density, taking into account the self-heating process (thermo field regime: $J_e(F,T)$) or not (pure field regime: $J_e(F,300\ K)$). Once again, the y-axis is the same, but for a better readability, current densities have been scaled by a factor of 4 and 10 for $f = 2$ and $f = 1$ respectively, as indicated in bold in the legend. Note that the distributions are zoomed (dashed gray lines) on the area emitting 90% of the total current. These areas, translated into radial coordinates, are highlighted by red and blue hatches.

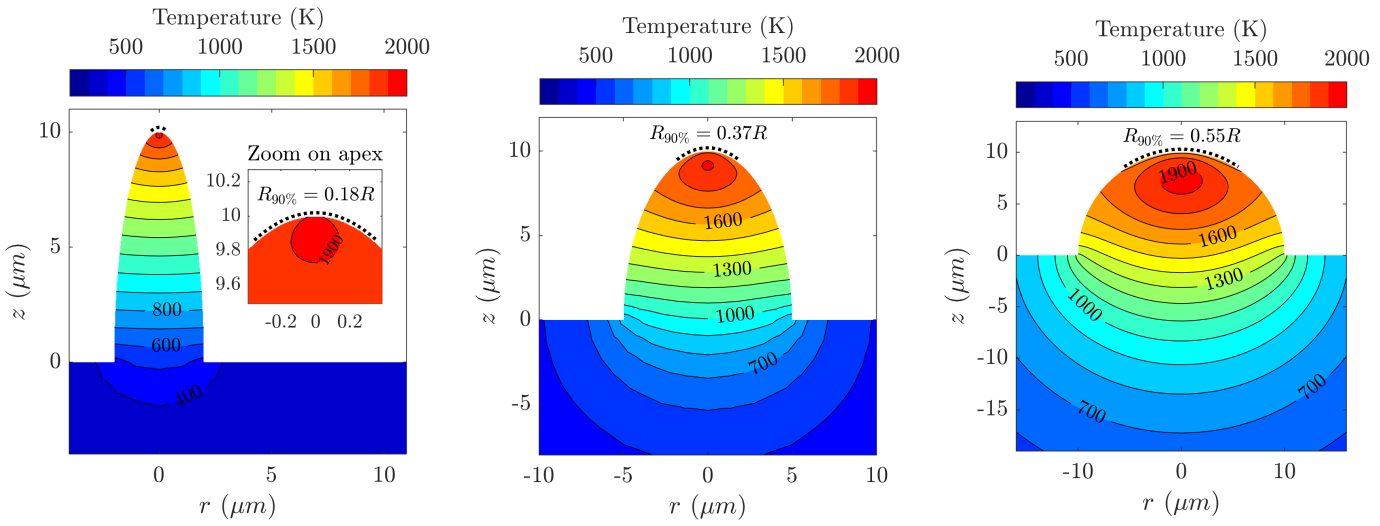

Fig. 7: Isothermal curves for the 2D axi-symmetric emission of single protrusions with aspect ratio $f = 5$, $f = 2$ and $f = 1$ when the corresponding pre-breakdown field E_0^{pb} is applied. The step between two successive isothermal curves is 100 K. The thick dotted lines above the protrusion apexes highlight the area contributing to 90% of the emitted current. $R_{90\%}$ is the corresponding radius.

the geometric curvature factor for an ellipsoid of height H and radius R, with $R = H/f$. One gets $R_{90\%} = 0.18R = 0.36\ \mu m$ for $f = 5$, $R_{90\%} = 0.37R = 1.85\ \mu m$ for $f = 2$ and $R_{90\%} = 0.55R = 5.5\ \mu m$ for $f = 1$. These results are highlighted on figure 6 *via* red hatches and on figure 7 *via* a thick black dotted line.

The overall lower electric field over the emission surface for smaller aspect ratios explains why rounder protrusions benefit more from thermo-field contribution (higher g_I at E_0^{pb}). Indeed, the influence of temperature on $J_e(F,T)$ predicted by the theory is precisely higher at lower field.

The larger emission area for smaller aspect ratio explains why their emitted current at pre-breakdown voltage is higher while their current densities are lower: approximately four times lower for $f = 2$ compared to $f = 5$, and ten times lower for $f = 1$, as highlighted in the legends of the current density graphs of figure 6. The emission area being larger for smaller aspect ratio, the Joule heating takes place over a larger volume beneath it. The increase of the volume temperature thus extends wider and can reach the surrounding of the protrusion basis. This is particularly visible for $f = 1$ and $f = 2$ on figure 7.

The question then arises as to whether this heat diffusion for low aspect ratio protrusions could significantly impact the emission of other protrusions in the vicinity. Characteristics of this possible thermal coupling is studied in the following section.

4. Investigation of thermal coupling between multiple protrusions

4.1. Phenomenology of interactions in 3D

So far, simulation results of single protrusions have been analysed. In real situation, as observed in electron sources or with surface roughness, the emitting protrusions are usually grouped. In such case, even though each emitter still might be assumed to have axial symmetry, the whole situation is not symmetric anymore. 3D modellings of the emission are required to account for the protrusions proximity. In the present work, two simplified arrangements are considered:

- A two identical protrusions arrangement separated by a distance d, named hereafter the *2IP arrangement* (figure 8a). *2IP* stands for *Two Indentical Protrusions*.
- An infinite 2D lattice of identical protrusions with a spacing distance d, named hereafter the *array arrangement* (figure 8b). The unit cell of the array is a $d \times d$ square. The whole arrangement is however modelled from a $\frac{d}{2} \times \frac{d}{2}$ square including a quarter of a protrusion, and using mirror symmetries at the lateral boundaries (figure 9).

In such configurations, the protrusions proximity induces electrostatic screening. This simple, well documented phenomenon [Dall'Agnol et al. 2018] – also named *mutual depolarization* [Forbes 2016] – reduces overall the field enhancement capability of the protrusions and consequently the local electric field around the apex. This effect is here quantified by the relative loss of the apex electric field δ_a:

$$\delta_a = \frac{F_a - \beta_a E_0}{\beta_a E_0} \tag{19}$$

where F_a is the actual electric field at the apex of the interacting protrusion (*i.e.* with screening) and $\beta_a E_0$ corresponds to the apex electric field for a single *isolated protrusion* (*i.e.* without screening). Due to the exponential decrease of the emitted current with smaller electric field, even a small field loss induces a noticeable current loss. This is particularly troublesome for electron sources, leading to a lot of studies about the spacing optimization in Field Emitters Array (FEA) [Bieker et al. 2017; Cai and Liu 2013; de Assis et al. 2020]. However, these studies do no take into account thermal effects in their search for an optimal spacing.

In the thermo-field regime, electrostatic screening reduces the emitted current and therefore reduces the self-heating process as well. As an example, figure 10 compares for $f = 1$ the temperature map of a single protrusion (figure 10a) and this of a 2IP arrangement with $d = 3R$ (figure 10b) under the same applied electric field: $E_0 = 1.9\ GV/m$. The decrease of the maximum temperature from 1941 K to 1471 K reveals a significant self heating reduction for a field loss at the apex of $\delta_a = -2.5\%$ only. As a consequence of this electrostatic screening, close protrusions need a higher electric field to reach the thermo-field regime.

It is however remarkable that a second effect, also related to proximity, slightly compensates the temperature decrease caused by screening. This is what is here referred to as *thermal coupling* and is highlighted on figure 10b by the joining of the isothermal curves in the cathode below the protrusions. An indirect way to evaluate its influence on temperature – and so on current – is to systematically compare two sets of independent simulation results. A first set corresponds to a normal simulation in 3D, accounting for both electrostatic screening and thermal coupling. For the second set, the electrostatics are first solved in 3D to account for the screening, but the heating process is then treated independently for each protrusion[4]. Proceeding this way artificially cancels the thermal coupling. The corresponding results are thus labelled *thermal coupling off* (TC-off) while the results of the first set are labelled *thermal coupling on* (TC-on). The consequence of cancelling the thermal coupling for the previous example is shown on figure 10c. It highlights a loss of 35 K in the maximum temperature and about 100 K in the temperature at the protrusion base compared to figure 10b, highlighted by the position of the isothermal curve at 700 K (displayed in white). Although this is a rather small variation, the thermal coupling is clearly shown on this example.

In fact, the small magnitude of thermal coupling is due to the electrostatic screening. To support this statement, a third simulation is performed. It independently solves the electrostatics for each protrusions alone and uses then the resulting surface electric field to simulate the heating process once including all protrusions. This procedure artificially cancels the electrostatic screening and the corresponding results are labelled *electrostatic screening off* (SC-off). The consequence is shown on figure 10d which is to be compared with the single protrusion case (10a). The effect of thermal coupling without screening are here roughly twice higher: the maximum temperature increases by 70 K and the increase at the protrusion bases is rather around 200 K.

This example gives insights into the phenomenology of thermal coupling. More details on the parameter dependence of thermal coupling are given in the following.

[4] In the considered 2IP and array arrangements, all the protrusions being equivalent, the heating process is solved only once. However, although there is only one protrusion, it is still solved in 3D as the surface electric field is no longer axi-symmetric due to screening.

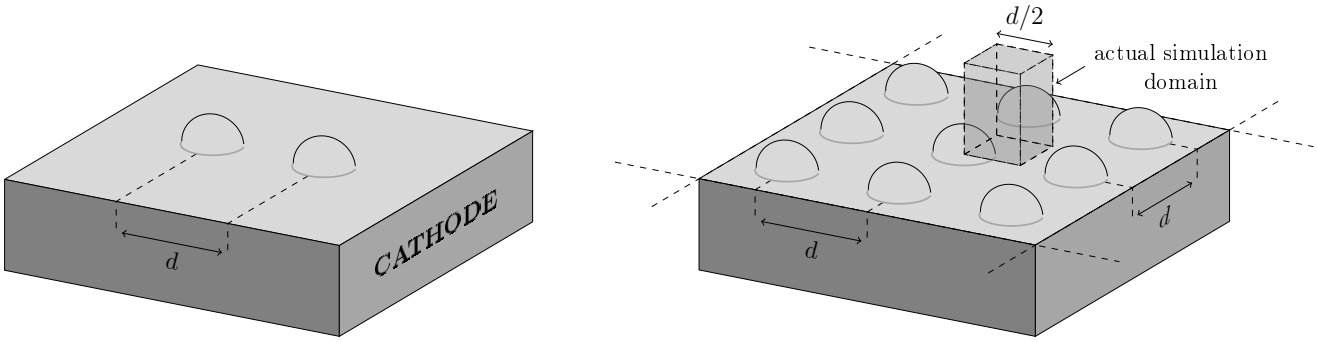

(a) Two identical protrusions separated by a distance d (2IP arrangement).

(b) Infinite square array of indentical protrusions with spacing distance d (array arrangement).

Fig. 8: Scheme of the two 3D arrangements considered in this work (example with $f = 1$). Scheme not at scale.

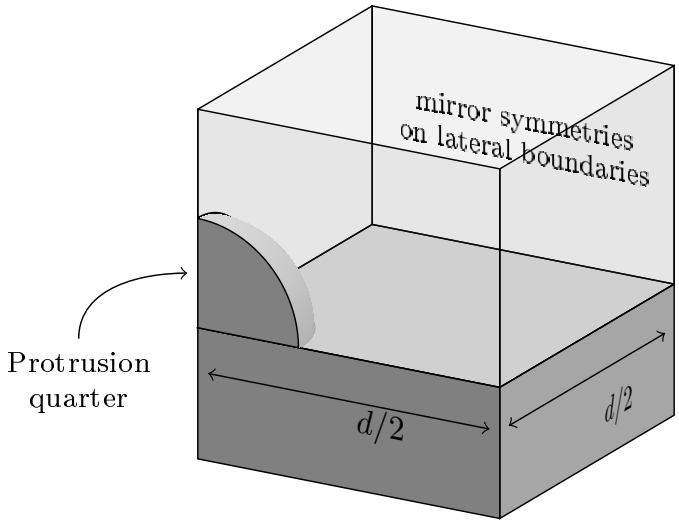

Fig. 9: Scheme of the actual simulation domain for the array arrangement. The mirror symmetries on the lateral boundaries reproduce the physics of an infinite square array of identical protrusions with spacing d.

4.2. Parametric analysis of thermal coupling

The goal of this subsection is to explore the parameters that influences thermal coupling and find the range that maximises the effect on current. *A priori*: rounded protrusions, close to breakdown, densely distributed so that they heat each other but spaced enough so that the screening does not suppress the emission. Because this work aims at finding an upper limit to this phenomenon, analyses are first performed on protrusions with an aspect ratio of 1, as dome-like protrusions were shown in section 3 to be the most favourable case for the heating of the cathode and the contribution of temperature to the current. This is also the reason why the array arrangement was chosen – in addition to the 2IP arrangement which is the easiest arrangement of multiple protrusions. Nevertheless, $f = 1$ protrusions require a particularly high applied electric field to emit in the thermo-field regime ($E_0 > 1$ GV/m). The following analysis should therefore be considered as a theoretical investigation of the thermal coupling phenomenon, in the range of parameters that maximizes it. Subsection 4.3 will be dedicated to results and discussion on more practical situations.

To get a quantitative evaluation of thermal coupling influence on the emitted current, both TC-on and TC-off sets are compared: the discrepancy between the current per protrusion in both sets, respectively I_{on} and I_{off}, is denoted ε_I and writes:

$$\varepsilon_I = \frac{I_{\text{on}} - I_{\text{off}}}{I_{\text{on}}} \tag{20}$$

Because I_{on} is taken as the reference, ε_I is a measure of the contribution of thermal coupling to the current. For instance, $\varepsilon_I = 4\%$ means 4% of the current I_{on} is due to thermal coupling. In order to get an upper limit, the aim is to find for both the 2IP and the array arrangement the distance d that maximizes ε_I. The results are compared on figure 11 for an applied electric field $E_0 = E_0^{\text{pb}}(f = 1) = 1.9$ GV/m, *i.e.* an apex electric field $F_a = \beta_a E_0 = 5.6$ GV/m.

Firstly, it is important to note the significant difference in screening between these two arrangement. The screening effect appears to be much higher for the array than for the 2IP arrangement. This is understandable as an infinite array becomes quite close to a flat surface when all the tips are in contact. For the array arrangement, when contact between the protrusions is reached, on the one hand, the maximum field loss is $\delta_a = -33\%$. The emitted current consequently drops from 3.55 A to 2 mA only. No temperature increase is produced in this case, and thermal coupling is null. Beyond $16R$ on the other hand, no more field loss nor thermal coupling is possible and the system behaves like a sum of isolated protrusions. Therefore, the spacing d maximizing the thermal coupling is reached for a compromise in distance, here $d = 5R$, still allowing the heat fluxes to couple while preventing a too high screening: $\delta_a = 5.2\%$ allowing a current of 1.3 A, in the thermo-field regime, of which 13% are due to thermal coupling.
For the 2IP arrangement, the maximum field loss does not exceed −4.7%. The maximum coupling can thus be reached when the two protrusions are in contact. The emitted current $I = 1.2$ A is similar to the array, but thermal coupling contributes here for 3.5% only. A higher impact of thermal coupling was found for the array arrangement, as expected: the more crowded the protrusions, the smaller the dissipation volume.
Overall, however, the observed values for $\varepsilon_I^{\max}$ are rather small in both cases since, having been obtained for $f = 1$, they are assumed to be upper limits. This confirms that when dealing with thermo-field emission, the thermal coupling due to protrusions proximity only has a second order effect on the

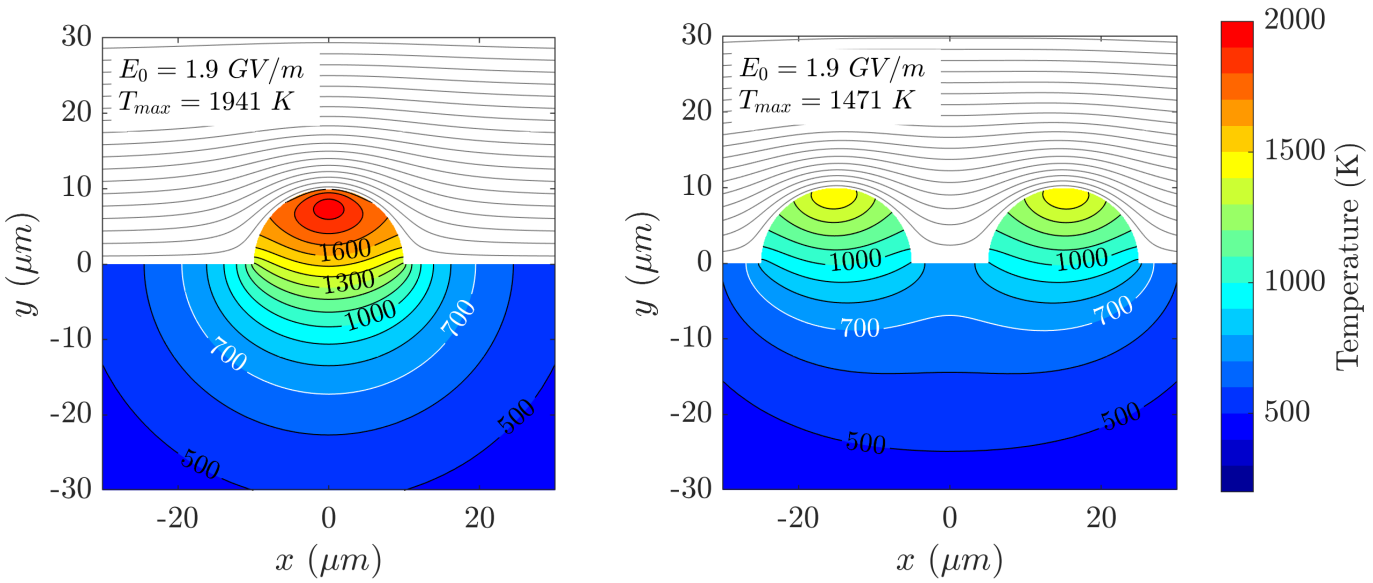

(a) Case of a single protrusion with $f = 1$.

(b) Case of two identical protrusions (2IP) with $f = 1$ and $d = 3R$.

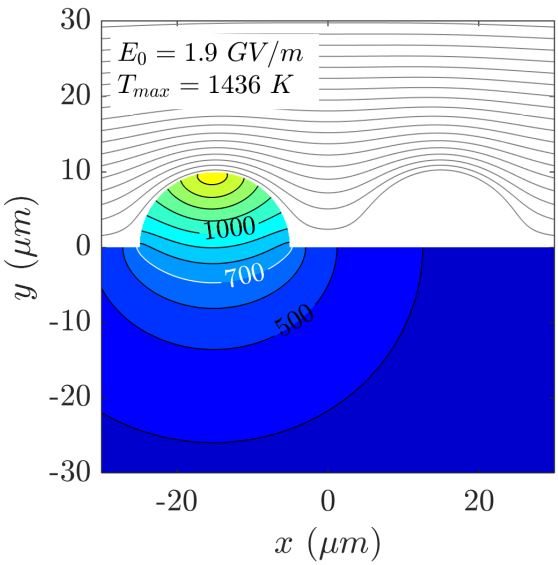

(c) Case of two identical protrusions (2IP) with $f = 1$ and $d = 3R$ with thermal coupling artificially cancelled (TC-off).

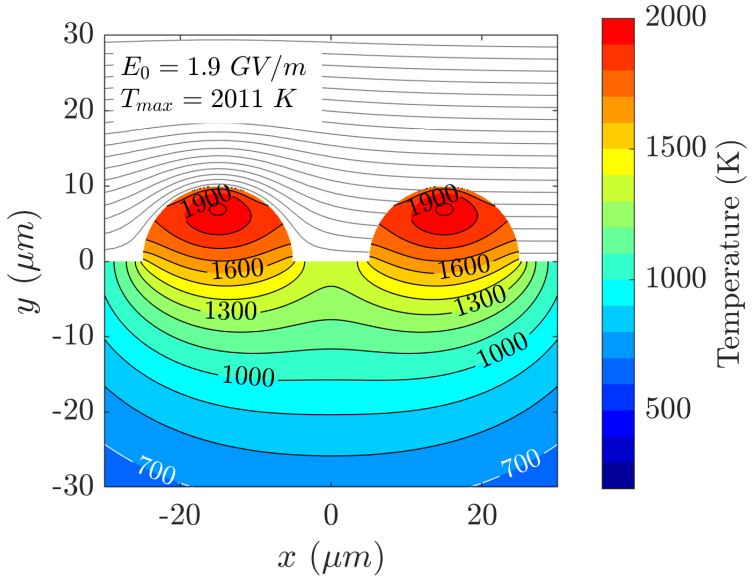

(d) Case of two identical protrusions (2IP) with $f = 1$ and $d = 3R$ with electrostatic screening artificially cancelled (SC-off).

Fig. 10: Isothermal curves (lower black lines with colormap) and equipotential curves (upper gray lines) at applied field $E_0 = E_0^{pb}(f = 1)$.

emitted electrons. The electrostatic screening plays the major role and prevents a significant thermal coupling. In fact, by artificially cancelling the screening in the simulations, all else being equal (results not shown), the contribution of thermal coupling gets roughly doubled: ε_I at $2R = 7.9\%$ for the 2IP arrangement and ε_I at $5R = 25\%$ for the array arrangement (not being the maximum anymore).

To go further, one can search for the maximum current discrepancies ε_I^{max} over d for higher f and analyse their behaviour. The results are limited to the array arrangement as the thermal coupling for a more sparse arrangement – all else being equal – would be smaller. As for $f = 1$ (see the graphs of figure 11), pairs of simulations with (TC-on) and without (TC-off) thermal coupling are performed for higher f over a wide range of array spacing d, with a sampling step equal to the protrusion radius R. The applied electric field corresponds respectively to the pre-breakdown field of each aspect ratio found in section 3 (figure 5). The value for ε_I^{max} is obtained from the pair exhibiting the highest current discrepancy, and the corresponding spacing at maximum is denoted d_*. Results are reported on figure 12, and in table 2 along with the field values, spacings at maximum, and maximum temperatures. It is observed that the thermal coupling contribution to the current quickly becomes negligible for higher

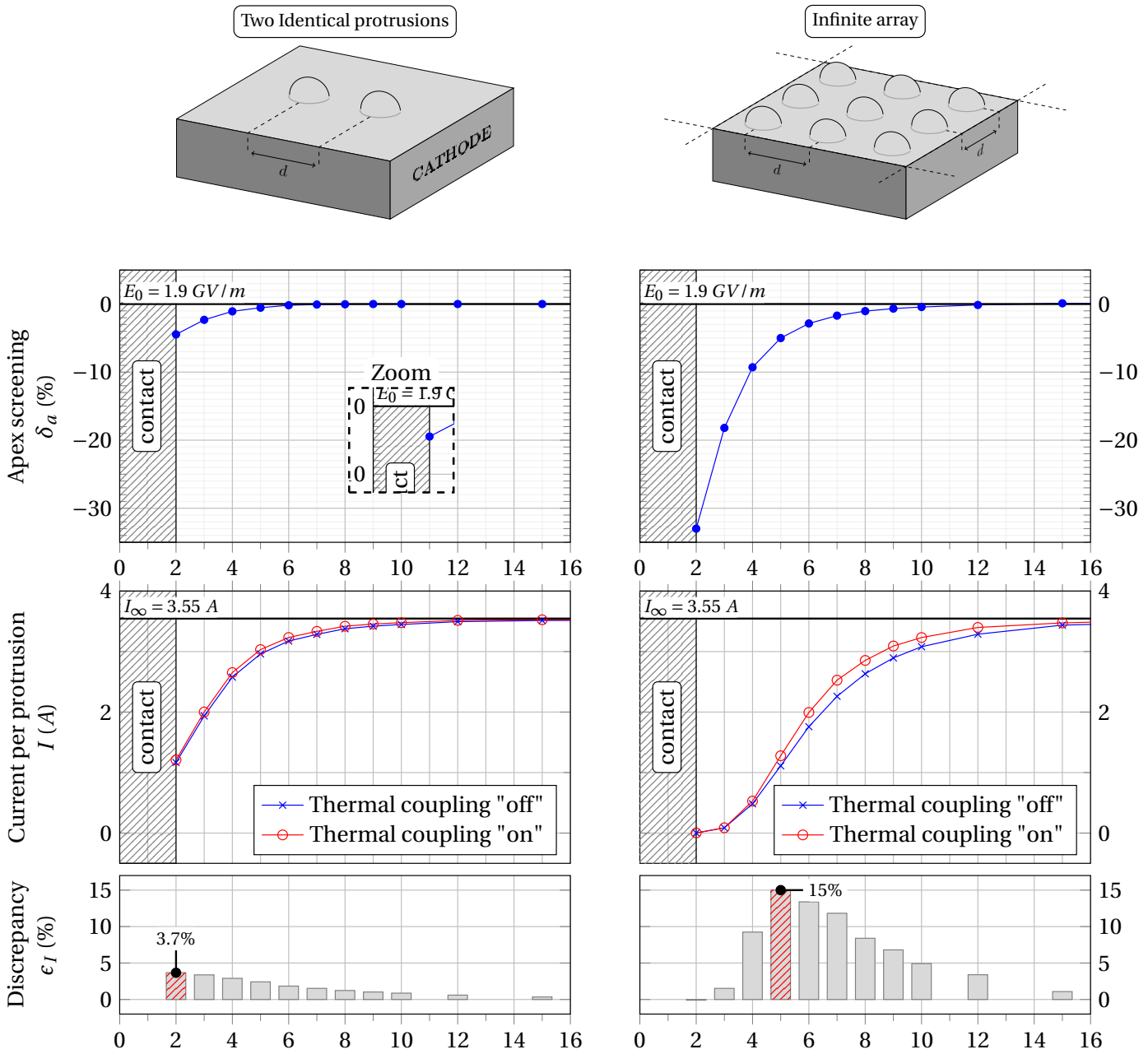

Fig. 11: Comparison of the influence of thermal coupling on the emitted current per protrusion between the 2IP and the array arrangement for $f = 1$. The x-axis corresponds to spacing distances d ranging from 2 to 16 protrusions radii and is the same for all graphs. The first row presents the screening efficiency at the apex δ_a. The middle row compares the emitted current with and without thermal coupling and the bottom row exhibits the discrepancy between those two cases. This discrepancy is in fact the percentage of emitted current that is due to the thermal coupling between the protrusions (ε_I). The maximum discrepancy over the tested distance d is highlighted by red hatches, and is denoted $\varepsilon_I^{\max}$.

aspect-ratio: from a maximum contribution over d of 13% for $f = 1$, $\varepsilon_I^{\max}$ drops to 2.2% for $f = 4$. In fact, as observed in figure 7, sharper protrusions dissipate their heat over a smaller distance at their bases. Thermal coupling can therefore only occur for shorter array spacing, where the higher electrostatic screening reduces the thermo-field emission. This assertion is supported by the spacing at maximum that decreases from 50 μm for $f = 1$ to 25 μm for $f = 4$, almost doubling the apex field loss: from -5.23% to -10.6% (table 2).

For $f > 4$ (results not shown), thermal coupling becomes too weak to be observed at large distances ($> 30\ \mu m$), and is suppressed by electrostatic screening at small distances ($< 25\ \mu m$). In between, several local maxima appear as different trade-off between a higher proximity or a smaller screening. Overall, these maxima correspond to negligible contribution to the current, $\epsilon_I < 2\%$, and disappear for $f > 8$.

These results highlight the difficulty to observe a thermal coupling between sharp protrusions. However, the applied voltage was here limited to the pre-breakdown voltage of *isolated protrusions*. With neighbouring protrusions in interaction, because of electrostatic screening, the system in fact requires a higher applied electric field for the protrusions to reach an equivalent thermal situation. The actual maximum temperature for the data of figure 12 are below the fusion temperature: $T_{\max}^{\text{on}} =$

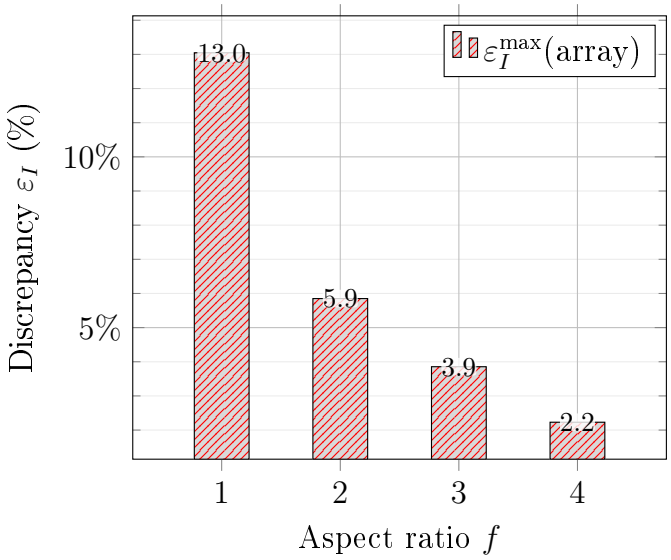

Fig. 12: Variation with the aspect ratio of the thermal coupling contribution to the current ε_I. For each aspect ratio, the chosen array spacing d is the one maximizing ε_I. The corresponding array spacings are given in table 2 along with the field values and the maximum temperatures.

Quantity	Unit	$f = 1$	2	3	4
β_a	–	3.0	5.8	9.2	13.3
E_0	GV/m	1.9	1.1	0.72	0.52
d_*/R	–	5	7	9	10
d_*	μm	50	35	30	25
δ_a	%	−5.23	−7.71	−7.89	−10.6
F_a	GV/m	5.32	5.73	6.08	6.13
$T_{\max}^{\text{off}}$	K	1167	1100	1171	923
$T_{\max}^{\text{on}}$	K	1316	1187	1229	962
$\varepsilon_I^{\max}$	%	13.0	5.9	3.9	2.2

Table 2: Relevant quantities for the field values, array spacings and maximum temperatures corresponding to the results of figure 12. The different quantities are defined in the manuscript. The height H for all protrusions is 10 μm.

1316 K for $f = 1$ and $T_{\max}^{\text{on}} = 962$ K only for $f = 4$ (table 2). By ramping up the voltage to its effective pre-breakdown value, the values of ε_I for high aspect ratio could then become noticeable. It is therefore hard to set an upper limit on thermal coupling magnitude without setting an upper limit on the applied electric field. This issue is discussed in what follows.

4.3. About the magnitude of thermal coupling in experiment-like situations

In modelling, physical processes can be isolated from one another. In addition, there is no intrinsic limit to the magnitude of the parameters. In experiments, however, the magnitude of the applied electric field usually ranges well below the gigavolt per meter. On the one hand, indeed, the maximum voltage delivered by the generators is limited. On the other hand a wide variety of physical processes can couple and cause breakdown at lower field values than the ones predicted only by the vaporization of an idealized micro-metric protrusion. In fact, in experiments concerning field electron sources, the applied field usually ranges from several volts per micrometers for the modern highly enhancing structures such as carbon nanotubes ($E_0 \gtrsim 10^6$ V/m), to a few tenth of gigavolt per meter for less sharp structures ($E_0 \gtrsim 10^8$ V/m) [Li et al. 2015]. In the case of high-gradient accelerating structures, modern linear accelerators such as CLIC – the Compact Linear Collider at CERN – operate with RF fields, around the 100 MV/m range [Wang et al. 2012]. Several experimental studies evaluate the high-voltage resistance of accelerators in DC mode and exhibit breakdown fields from 100 to 800 MV/m [Descoeudres et al. 2009].

With these values in mind, here is finally investigated the magnitude of thermal coupling under a purposefully borderline field of 0.4 GV/m. Under this field restriction, the upper limit of ε_I over our parameter range is estimated. Referring to the third panel of figure 5 in section 3, extracting current via thermo-field emission at 0.4 GV/m from protrusions with $f < 5$, *i.e.* $\beta_a < 17.9$ is not possible. Hemiellipsoids from which a current can be extracted have an aspect ratio $f \geq 5$. Therefore, a final series of simulations is performed for $f = 5$ to 10 with E_0 fixed to 0.4 GV/m. Note that this value is much higher than the pre-breakdown voltage of *isolated protrusions* of aspect ratio $f > 5$. In an array arrangement, however, because of the electrostatic screening, there exists for each of these aspect ratios a unique spacing distance for which the maximum temperature in the protrusions reaches the fusion temperature. In analogy to our definition of the pre-breakdown voltage V_{pb}, this *pre-breakdown spacing* is denoted d_{pb}. For this specific spacing, two sets of simulation in the array arrangement are compared following the method described previously: the first set takes into account the thermal coupling while this phenomenon is artificially cancelled for the second set. The relevant results for the comparison are summarized in table 3.

Obviously, because sharper protrusions have a higher apex field enhancement factor (denoted as β_a), they can emit in the thermo-field regime while undergoing a higher screening than low aspect ratio protrusions. This is why the distance d_{pb} is smaller for higher f. For example, for $f = 6$ the pre-breakdown is reached at $d_{\text{pb}} = 16.1$ μm with a screening of $\delta_a = -21.5\%$, while for $f = 10$, $d_{\text{pb}} = 5.8$ μm is smaller, inducing a roughly three times higher apex field loss, $\delta_a = -60.4\%$. Despite the smaller impact of thermal effects for sharper protrusions exposed in section 3, the applied electric field of 0.4 GV/m allows a higher proximity for higher f, enhancing further the influence of thermal coupling for $f = 10$: $\varepsilon_I = 14.5\%$ than for $f = 6$: $\varepsilon_I = 6.2\%$. This remarkable result confirms that the main obstacle to a noticeable contribution of thermal coupling to thermo-field emission is the electrostatic screening. When the latter phenomenon is counterbalanced by a high enough applied field, the contribution of thermal coupling can be noticeable. In the present case, $\varepsilon_I \gtrsim 10\%$ with $d \lesssim H$ for sharp protrusions with apex FEF corresponding to regular field emitters characterized by $20 < \beta_a < 50$. Such configurations can be observed in Field Emitter Arrays (FEA) experiments where the emitters are grown densely packed (as for example in [Spindt 1992] section 4.1 therein). The above results thus suggest that a small part (up to $\sim$ 15% here) of the extracted current in these configurations at applied voltage close to the pre-breakdown voltage could be assigned to a thermal coupling by the bulk between neighbouring emitters.

Quantity	Unit	$f = 5$	6	7	8	9	10
β_a	–	17.9	23.1	28.9	35.2	42.0	49.3
E_0	GV/m			0.4			
d_{pb}/R	–	25.0	9.7	7.1	7.0	6.3	5.8
d_{pb}	μm	50.0	16.1	10.1	8.7	7.0	5.8
δ_a	%	-1.3	-21.5	-36.1	-46.5	-54.5	-60.4
F_a	GV/m	7.01	7.25	7.39	7.53	7.64	7.81
$T^{\text{off}}_{\text{max}}$	K	1907	1887	1840	1844	1789	1791
$T^{\text{on}}_{\text{max}}$	K			T_M : 1941 $K \pm 1\%$			
I_{off}	mA	103.3	63.3	38.9	27.5	18.6	14.3
I_{on}	mA	106.0	67.5	42.6	30.2	20.9	16.7
ε_I	%	2.5	6.2	9.0	8.9	11.0	14.5

Table 3: Comparison at the pre-breakdown distance d_{pb} of the maximum temperature and emitted current between a set that takes into account the thermal coupling ($T^{\text{on}}_{\text{max}}$, I_{on}) and a set that artificially cancels thermal coupling ($T^{\text{off}}_{\text{max}}$, I_{off}). The corresponding contribution of thermal coupling to the current (ε_I) is given. The apex field F_a and apex field loss δ_a are displayed as well for more clarity. The comparison is limited to protrusions with aspect ratio f from 10 to 5, as no thermo-field emission is possible for rounder protrusions ($f < 5$) under an applied electric field $E_0 = 0.4\ GV/m$. The protrusions height is $10\ \mu m$.

As final words, it is interesting to note that, beyond thermal coupling, taking into account thermal effects to roughly estimate the pre-breakdown voltage changes a lot the studies aimed at optimizing spacing in FEA. Indeed, computing the temperature is a reasonable way to evaluate the maximum applied electric field under which an FEA electron source can operate without failure. In addition, it is important to take into account the gain in current due to the temperature. From these considerations, a densely packed distributions of sharp tips emitting in the thermo-field regime under a high applied electric field, that compensates for the screening but do not causes breakdown, can lead to a better emitted current per unit surface than an *electrostatics-only* optimized distribution of the same emitters.
Taking an example from the present work, the emitted current per protrusion for $f = 10$ under $0.4\ GV/m$ in the array arrangement with spacing $d_{\text{pb}} = 5.8\mu m$ (table 3) is the same, $I = 17\ mA$, than that of an isolated protrusion of $f = 10$ under $0.16\ GV/m$ (figure 5). In terms of current per unit surface however, an array of 'isolated' protrusions with $f = 10$ requires at least a spacing of $50\ \mu m$ (to have $\delta_a < 1\%$) which gives $I/d^2 = 6.8 \times 10^6\ A/m^2$ while the array arrangement being more dense delivers a higher current per unit surface, $I/d^2 = 5.1 \times 10^8\ A/m^2$, despite a strong apex electric field loss $\delta_a = -60.4\%$.

5. Conclusion

This modelling work deals with thermo-field electron emission (TFE) from idealized protrusions. It focuses on hemiellipsoids with aspect ratios $f = H/R$ from 10 to 1 in order to model protrusions ranging from typical electron source emitters with notable apex field enhancement factors, $\beta_a \sim 50$, to simple surface asperity with low apex FEF, $\beta_a \sim 3$. A size of $H = 10\ \mu m$ was chosen, but the results are consistent over variations of a few micrometers.

The transition from pure field regime to thermo-field regime over the applied electric field is characterized for the given set of protrusions. The variations of the temperature influence on the emitted current are analysed: at pre-breakdown voltage, the self-heating of protrusions demonstrates significant gains in current, ranging from +60% for $f = 10$ to +110% for $f = 1$. These maximum values outline the influence of temperature when dealing with breakdown problems in electron sources or high-voltage devices. It also highlights the need to account for thermal effect in the modelling studies aimed at optimizing spacing in Field Emitter Array (FEA). In addition, it is observed that thermal contribution is higher for rounder protrusions, with smaller apex FEF. Through the analysis of local variable distributions, this result is attributed to the protrusions geometry: for smaller aspect ratio, an overall smaller local electric field spread over a wider emission area is responsible for a higher contribution of temperature to the current.

Colormaps of the temperature distribution at equilibrium are shown at the pre-breakdown voltage for isolated protrusions. They give insights into the way protrusions of different shapes – here, different aspect ratios – heats up all over their volume until the melting point is reached. Besides, in line with previous works, our results show how a cooling Nottingham effect at the protrusion apex affects the equilibrium temperature distribution. This causes the highest temperature to be found not at the apex of the emitter but slightly below. The fusion temperature being reached underneath the emitter surface, this could be related to an explosive breakdown phenomena as reported in several experimental studies.

These temperature maps obtained at pre-breakdown also demonstrate a significant heating of the cathode bulk around their bases. This observation supports the possibility of a thermal coupling between close protrusions via the bulk material on which they are located. In the thermo-field regime, modelling results for multiple protrusions in interaction demonstrate the effect of a thermal coupling from the base, up to a contribution to the current ε_I of 13%. This maximum value is obtained for the smallest aspect ratio considered, $f = 1$. Indeed the heat around their bases was observed to spread wider for protrusions with lower aspect ratio. It should be noted, however, that the value of the pre-breakdown field for such dome-like protrusion ($f = 1$) is out of the experimental range. For sharper protrusions, emitting at lower applied electric field, the heat spreads over a smaller distance. The self-heating process for protrusions interacting at these smaller distances is drastically reduced by the electric field loss around the apex, therefore preventing any thermal coupling at their bases. The overall weak influence of thermal coupling on the emission is in fact related to the prevalence of the electrostatic screening when protrusions are densely distributed.

Nevertheless, for specific configurations achievable in Field Emitter Array experiments, the electrostatic screening can be compensated by a higher applied electric field. A parametric study at a borderline applied electric field of $0.4\ GV/m$ demonstrates noticeable thermal couplings ($\varepsilon_I > 5\%$) for protrusions sufficiently enhancing the electric field: $f > 5$, $\beta_a > 20$. An upper value of $\varepsilon_I = 14.5\%$ is observed for an array arrangement of protrusions with $f = 10$ and a spacing distance of $5.8\mu m$.

References

M. G. Ancona. Thermomechanical analysis of failure of metal field emitters. *Journal of Vacuum Science & Technology B: Microelectronics and Nanometer Structures*, 13(6):2206, Nov. 1995. ISSN 0734211X. . 2, 7

A. Batrakov, D. Proskurovsky, and S. Popov. Observation of the field emission from the melting zone occurring just before explosive electron emission. *IEEE Transactions on Dielectrics and Electrical Insulation*, 6(4):410–417, Aug. 1999. ISSN 10709878. . 5

J. Bieker, F. Roustaie, H. F. Schlaak, C. Langer, and R. Schreiner. Field emission characterization of in-situ deposited metallic nanocones. In *2017 30th International Vacuum Nanoelectronics Conference (IVNC)*, pages 120–121, July 2017. . 9

G. S. Bocharov and A. V. Eletskii. Thermal instability of field emission from carbon nanotubes. *Technical Physics*, 52(4):498–503, Apr. 2007. ISSN 1063-7842, 1090-6525. . 2

D. Cai and L. Liu. The screening effects of carbon nanotube arrays and its field emission optimum density. *AIP Advances*, 3(12):122103, Dec. 2013. ISSN 2158-3226. . 9

F. M. Charbonnier, R. W. Strayer, L. W. Swanson, and E. E. Martin. Nottingham Effect in Field and T - F Emission: Heating and Cooling Domains, and Inversion Temperature. *Physical Review Letters*, 13(13):397–401, Sept. 1964. ISSN 0031-9007. . 2, 3

COMSOL. Detailed Explanation of the Finite Element Method (FEM). https://www.comsol.com/multiphysics/finite-element-method, 2020. 2, 4

F. F. Dall'Agnol, T. A. de Assis, and R. G. Forbes. Physics-based derivation of a formula for the mutual depolarization of two post-like field emitters. *Journal of Physics: Condensed Matter*, 30(37):375703, Sept. 2018. ISSN 0953-8984, 1361-648X. . 9

D. K. Davies and M. A. Biondi. Mechanism of dc Electrical Breakdown between Extended Electrodes in Vacuum. *Journal of Applied Physics*, 42(8):3089–3107, July 1971. ISSN 0021-8979, 1089-7550. . 5

T. A. de Assis, F. F. Dall'Agnol, and M. Cahay. Universal trade-off between proximity and aspect-ratio in optimizing the field enhancement factor of large area field emitters. *Applied Physics Letters*, 116(20):203103, May 2020. ISSN 0003-6951, 1077-3118. . 9

A. Descoeudres, T. Ramsvik, S. Calatroni, M. Taborelli, and W. Wuensch. Dc breakdown conditioning and breakdown rate of metals and metallic alloys under ultrahigh vacuum. *Physical Review Special Topics - Accelerators and Beams*, 12(3):032001, Mar. 2009. . 13

W. P. Dyke, J. K. Trolan, W. W. Dolan, and G. Barnes. The Field Emitter: Fabrication, Electron Microscopy, and Electric Field Calculations. *Journal of Applied Physics*, 24(5):570–576, May 1953a. ISSN 0021-8979, 1089-7550. . 2

W. P. Dyke, J. K. Trolan, E. E. Martin, and J. P. Barbour. The Field Emission Initiated Vacuum Arc. I. Experiments on Arc Initiation. *Physical Review*, 91 (5):1043–1054, Sept. 1953b. ISSN 0031-899X. . 4

R. G. Forbes. Physical electrostatics of small field emitter arrays/clusters. *Journal of Applied Physics*, 120(5):054302, Aug. 2016. ISSN 0021-8979. . 9

R. H. Fowler and L. Nordheim. Electron emission in intense electric fields. *Proc. R. Soc. Lond. A*, 119(781):173–181, May 1928. ISSN 0950-1207, 2053-9150. . 2

G. N. Fursey. Field Emission and Vacuum Breakdown. *IEEE Transactions on Electrical Insulation*, EI-20(4):659–670, Aug. 1985. ISSN 0018-9367. . 5

C. Y. Ho, R. W. Powell, and P. E. Liley. Thermal Conductivity of the Elements. *Journal of Physical and Chemical Reference Data*, 1(2):279–421, Apr. 1972. ISSN 0047-2689, 1529-7845. . 5

A. Kyritsakis and J. P. Xanthakis. Extension of the general thermal field equation for nanosized emitters. *Journal of Applied Physics*, 119(4):045303, Jan. 2016. ISSN 0021-8979, 1089-7550. . 3

Y. Li, Y. Sun, and J. T. W. Yeow. Nanotube field electron emission: Principles, development, and applications. *Nanotechnology*, 26(24):242001, June 2015. ISSN 0957-4484, 1361-6528. . 13

W. I. Milne, K. B. K. Teo, E. Minoux, O. Groening, L. Gangloff, L. Hudanski, J.-P. Schnell, D. Dieumegard, F. Peauger, I. Y. Y. Bu, M. S. Bell, P. Legagneux, G. Hasko, and G. A. J. Amaratunga. Aligned carbon nanotubes/fibers for applications in vacuum microwave amplifiers. *Journal of Vacuum Science & Technology B: Microelectronics and Nanometer Structures*, 24(1):345, 2006. ISSN 10711023. . 1

N. D. Milošević and K. D. Maglić. Thermophysical properties of solid phase titanium in a wide temperature range. *High Temperatures-High Pressures*, 37 (3):187–204, Jan. 2008. 5

E. Minoux, O. Groening, K. B. K. Teo, S. H. Dalal, L. Gangloff, J.-P. Schnell, L. Hudanski, I. Y. Y. Bu, P. Vincent, P. Legagneux, G. A. J. Amaratunga, and W. I. Milne. Achieving High-Current Carbon Nanotube Emitters. *Nano Letters*, 5(11):2135–2138, Nov. 2005. ISSN 1530-6984, 1530-6992. . 4

E. L. Murphy and R. H. Good. Thermionic Emission, Field Emission, and the Transition Region. *Physical Review*, 102(6):1464–1473, June 1956. ISSN 0031-899X. . 2

W. B. Nottingham. Remarks on Energy Losses Attending Thermionic Emission of Electrons from Metals. *Physical Review*, 59(11):906–907, June 1941. ISSN 0031-899X. . 2

P. Rossetti, F. Paganucci, and M. Andrenucci. Numerical model of thermoelectric phenomena leading to cathode-spot ignition. *Ieee Transactions on Plasma Science*, 30(2):1561–1567, Aug. 2002. ISSN 0093-3813. . 2

S. Sarkar and D. Biswas. Electrostatic field enhancement on end-caps of cylindrical field-emitters. *Journal of Vacuum Science & Technology B*, 37(6):062203, Nov. 2019. ISSN 2166-2746, 2166-2754. . 1

B. Seznec, P. Dessante, L. Caillault, J.-L. Babigeon, P. Teste, and T. Minea. Controlled electron emission and vacuum breakdown with nanosecond pulses. *Journal of Physics D: Applied Physics*, 49(23):235502, June 2016. ISSN 0022-3727, 1361-6463. . 5

B. Seznec, P. Dessante, P. Teste, and T. Minea. Effect of space charge on vacuum pre-breakdown voltage and electron emission current. *Paper Submitted for Publication to Journal of Physics D: Applied Physics*, 2020. 4

C. Spindt. Microfabricated field-emission and field-ionization sources. *Surface Science*, 266(1-3):145–154, Apr. 1992. ISSN 00396028. . 13

C. A. Spindt, C. E. Holland, I. Brodie, J. B. Mooney, and E. W. Westerberg. Field-Emitter Arrays Applied to Vacuum Fluorescent Display. *Le Journal de Physique Colloques*, 49(C6):C6–153–C6–154, Nov. 1988. ISSN 0449-1947. . 1

T. Su, C. Lee, and J.-M. Huang. Electrical and thermal modeling of a gated field emission triode. In *Proceedings of IEEE International Electron Devices Meeting*, pages 765–768, Washington, DC, USA, 1993. IEEE. ISBN 978-0-7803-1450-4. . 2, 7

W. Sugimoto, S. Sugita, Y. Sakai, H. Goto, Y. Watanabe, Y. Ohga, S. Kita, and T. Ohara. A fine-focusing x-ray source using carbon-nanofiber field emitter. *Journal of Applied Physics*, 108(4):044507, Aug. 2010. ISSN 0021-8979, 1089-7550. . 1

H. Timko, K. Ness Sjobak, L. Mether, S. Calatroni, F. Djurabekova, K. Matyash, K. Nordlund, R. Schneider, and W. Wuensch. From Field Emission to Vacuum Arc Ignition: A New Tool for Simulating Copper Vacuum Arcs. *Contributions to Plasma Physics*, 55(4):299–314, Apr. 2015. ISSN 08631042. . 1

T. Utsumi. Vacuum microelectronics: What's new and exciting. *IEEE Transactions on Electron Devices*, 38(10):2276–2283, Oct. 1991. ISSN 00189383. . 1

G. E. Vibrans. Vacuum Voltage Breakdown as a Thermal Instability of the Emitting Protrusion. *Journal of Applied Physics*, 35(8):4, 1964. . 2

J. Wang, SLAC, J. Lewandowski, SLAC, J. Van Pelt, SLAC, C. Yoneda, SLAC, B. Gudkov, CERN, G. Riddone, CERN, T. Higo, T. Kek, T. Takatomi, and T. Kek. Fabrication Technologies of the High Gradient Accelerator Structures at 100MV/M Range. *Conf.Proc.C100523:THPEA064,2010*, (SLAC-PUB-15146), July 2012. 13

Y. B. Zhu and L. K. Ang. Space charge limited current emission for a sharp tip. *Physics of Plasmas*, 22(5):052106, May 2015. ISSN 1070-664X, 1089-7674. . 4